FISFVIFR

Contents lists available at ScienceDirect

## **Engineering Fracture Mechanics**

journal homepage: www.elsevier.com/locate/engfracmech





# A cohesive XFEM model for simulating fatigue crack growth under various load conditions

R. Dekker a,\*, F.P. van der Meer a, J. Maljaars b,c, L.J. Sluys a

- <sup>a</sup> Faculty of Civil Engineering and Geosciences, Delft University of Technology, Delft, The Netherlands
- <sup>b</sup> Faculty of Built Environment, Eindhoven University of Technology, Eindhoven, The Netherlands
- <sup>c</sup> Structural Reliability, TNO, Delft, The Netherlands

#### ARTICLE INFO

Keywords: Fatigue crack growth XFEM Cohesive zone model Overload Mixed-mode Out-of-phase

## ABSTRACT

This study presents calibration and validation of a cohesive extended finite element model for fatigue crack propagation in ductile materials. The approach relies on a separation between plasticity around the crack tip and fatigue crack growth at the crack tip such that the influence of plasticity on fatigue driving forces is predicted. This implies that characterization of crack growth requires effective Paris parameters. It is shown that the calibrated model can capture fatigue crack growth behaviour in ductile materials for in-phase and out-of-phase biaxial fatigue loading as well as in-phase biaxial loading with an overload.

## 1. Introduction

Various structures such as vehicles, bridges and wind turbines, are subjected to cyclic loading. It is common that their fatigue crack propagation behaviour is simulated with models that are only valid for mode I constant amplitude loading. However, in reality, the applied cyclic loading can vary in direction, order and magnitude. Uncertainty on how these effects should be accounted for in computational models hampers an accurate fatigue life prediction.

In literature, most research beyond standard constant amplitude loading has been done for overloading and in-phase mixed mode loading. An overload can create a significant crack growth retardation effect, often attributed to plasticity induced crack closure [1–3]. On the other hand, a change in loading direction can cause a mixed-mode stress field around the crack tip, changing the crack growth direction [4,5].

The developed overload models generally make use of a cohesive zone [6–11]. The effect of an overload is captured by including plastic behaviour, either in the cohesive zone or in the bulk material. For these models, the calibration of parameters is generally not extensively discussed.

Mixed-mode loading models mainly utilize the eXtended Finite Element Method (XFEM) [12,13] to enable crack growth through elements [14–17]. However, only in-phase mixed-mode loading has been considered in such models whereas out-of-phase mixed-mode has mainly been limited to experimental research [5,18–20]. The research on modelling this behaviour is limited to an analysis of different crack path prediction methods [20,21].

In recent work, the authors have developed a thick level set model that can capture the effect of overloads by separating plasticity around the crack tip from fatigue crack growth at the crack tip [22]. Afterwards, this approach has been used for a cohesive XFEM model, employing the phantom node version of the XFEM [23–27], such that both the effects of overloading and mixed-mode loading can be captured [28]. In this model, a cohesive zone is used to approximate the damage behaviour in front of the physical

<sup>\*</sup> Correspondence to: PO Box 5048, 2600 GA Delft, The Netherlands. E-mail address: r.dekker-2@tudelft.nl (R. Dekker).

$\begin{array}{lll} a & \operatorname{Crack length} \\ b & \operatorname{Measure for the rate of change of the yield surface} \\ C & \operatorname{Linear kinematic hardening coefficient} \\ c, c_{\rm c}, c_{\rm p} & \operatorname{paris constant, elastic, plastic} \\ d & \operatorname{Damage} \\ E & \operatorname{Young's modulus} \\ f & \operatorname{Von Mises yield criterion} \\ G_{\rm c} & \operatorname{Critical energy release rate} \\ G, G_{\rm e}, G_{\rm p}, G^{\max}, G^{\min} & \operatorname{Energy release rate, elastic, plastic, maximum, minimum} \\ K & \operatorname{Stress intensity factor} \\ K_{\rm c} & \operatorname{Initial cohesive stiffness} \\ I_{\rm p} & \operatorname{Fracture process zone length} \\ I_{\rm w} & \operatorname{Weight function rate of decay} \\ M_{\rm mm, m_c, m_p} & \operatorname{paris exponent, elastic, plastic} \\ N & \operatorname{Number of cycles} \\ P, P_{\rm max} & \operatorname{Applied load, maximum} \\ Q_{\rm co} & \operatorname{Limit value for yield stress increase} \\ R & \operatorname{Radius} \\ F_{\rm w} & \operatorname{Weight function distance parameter} \\ W & \operatorname{Width} \\ w & \operatorname{Weighting value} \\ s & \operatorname{Deviatoric stress} \\ \beta & \operatorname{Mixed-mode strength ratio} \\ \gamma & \operatorname{Non-linear kinematic hardening coefficient} \\ \delta, \delta_{\rm f}, \delta_{\rm i}, \delta_{\rm m} & \operatorname{Effective displacement jump, final failure, initiation, maximum} \\ \delta_{\rm m}, \delta_{\rm s} & \operatorname{Normal and tangential displacement jump} \\ \epsilon^{\rm p} & \operatorname{Equivalent plastic strain} \\ v & \operatorname{Poisson ratio} \\ \xi & \operatorname{Deviatoric back-stress} \\ \sigma_{\rm y}, \sigma_{\rm o} & \operatorname{Yield stress, initial} \\ \tau & \operatorname{Effective cohesive traction} \\ \tau_{\rm max} & \operatorname{Tensile strength} \\ \tau_{\rm n, r}, \tau_{\rm s} & \operatorname{Normal and tangential cohesive traction} \\ \phi & \operatorname{Location parameter} \\ \end{array}$	Nomenclature						
C       Linear kinematic hardening coefficient         c, $c_e$ , $c_p$ Paris constant, elastic, plastic         d       Damage         E       Young's modulus         f       Von Mises yield criterion $G_c$ Critical energy release rate $G_s$ , $G_p$ , $G^{max}$ , $G^{min}$ Energy release rate, elastic, plastic, maximum, minimum         K       Stress intensity factor $K_c$ Initial cohesive stiffness $I_p$ Fracture process zone length $I_w$ Weight function rate of decay $m_m$ , $m_c$ , $m_p$ Paris exponent, elastic, plastic $N$ Number of cycles $P$ , $P_{max}$ Applied load, maximum $Q_\infty$ Limit value for yield stress increase $R$ Radius $r_w$ Weight function distance parameter $W$ Width $w$ Weighting value         s       Deviatoric stress $\beta$ Mixed-mode strength ratio $\gamma$ Non-linear kinematic hardening coefficient $\delta_n$ , $\delta_1$ , $\delta_m$ Effective displacement jump, final failure, initiation, maximum $\delta_p$ Plastic strain <t< th=""><th>a</th><th colspan="6">Crack length</th></t<>	a	Crack length					
c, $c_e$ , $c_p$ Paris constant, elastic, plastic         d       Damage         E       Young's modulus         f       Von Mises yield criterion $G_c$ Critical energy release rate $G_c$ Critical energy release rate, elastic, plastic, maximum, minimum $K$ Stress intensity factor $K_c$ Initial cohesive stiffness $l_p$ Fracture process zone length $l_w$ Weight function rate of decay $m$ , $m_e$ , $m_p$ Paris exponent, elastic, plastic $N$ Number of cycles $P$ , $P_{max}$ Applied load, maximum $Q_{\infty}$ Limit value for yield stress increase $R$ Radius $r_w$ Weight function distance parameter $W$ Width $w$ Weighting value $s$ Deviatoric stress $\beta$ Mixed-mode strength ratio $\gamma$ Non-linear kinematic hardening coefficient $\delta$ , $\delta_t$ , $\delta_t$ , $\delta_t$ Mormal and tangential displacement jump $\epsilon^p$ Plastic strain $\epsilon^p$ Equivalent plastic strain $\epsilon^p$ Equivalent plastic st	b						
$d$ Damage $E$ Young's modulus $f$ Von Mises yield criterion $G_c$ Critical energy release rate $G_c$ $G_c$ Critical energy release rate, elastic, plastic, maximum, minimum $K$ Stress intensity factor $K_c$ Initial cohesive stiffness $I_p$ Fracture process zone length $I_w$ Weight function rate of decay $m$ Number of cycles $N$ Number of cycles	C						
$d$ Damage $E$ Young's modulus $f$ Von Mises yield criterion $G_c$ Critical energy release rate $G_c$ Critical energy release rate, elastic, plastic, maximum, minimum $K$ Stress intensity factor $K_c$ Initial cohesive stiffness $I_p$ Fracture process zone length $I_w$ Weight function rate of decay $m$ Number of cycles $N$ Number of cycles $N$ Number of cycles $P$ $P_{max}$ Applied load, maximum $Q_{\infty}$ Limit value for yield stress increase $R$ Radius $r_w$ Weight function distance parameter $W$ Width $w$ Weighting value $s$ Deviatoric stress $\beta$ Mixed-mode strength ratio $\gamma$ Non-linear kinematic hardening coefficient $\delta$ $\delta_1$ $\delta_m$ $\delta$ Normal and tangential displacement jump $e^p$ Plastic strain $\delta$ Deviatoric back-stress $\sigma_y$ Opera	$c, c_{\rm e}, c_{\rm p}$						
$ f \qquad \text{Von Mises yield criterion} \\  G_{c} \qquad \text{Critical energy release rate} \\  G, G_{e}, G_{p}, G^{\text{max}}, G^{\text{min}}  \text{Energy release rate} \\  e, Stress intensity factor \\  K_{c} \qquad \text{Initial cohesive stiffness} \\  l_{p} \qquad \text{Fracture process zone length} \\  l_{w} \qquad \text{Weight function rate of decay} \\  m, m_{e}, m_{p} \qquad \text{Paris exponent, elastic, plastic} \\  N \qquad \text{Number of cycles} \\  P, P_{\text{max}} \qquad \text{Applied load, maximum} \\  Q_{\infty} \qquad \text{Limit value for yield stress increase} \\  R \qquad \text{Radius} \\  r_{w} \qquad \text{Weight function distance parameter} \\  W \qquad \text{Width} \\  w \qquad \text{Weighting value} \\  s \qquad \text{Deviatoric stress} \\  \beta \qquad \text{Mixed-mode strength ratio} \\  \gamma \qquad \text{Non-linear kinematic hardening coefficient} \\  \delta, \delta_{f}, \delta_{i}, \delta_{m} \qquad \text{Effective displacement jump, final failure, initiation, maximum} \\  \delta_{n}, \delta_{s} \qquad \text{Normal and tangential displacement jump} \\  e^{p} \qquad \text{Plastic strain} \\  \tilde{e}^{p} \qquad \text{Equivalent plastic strain} \\  \delta \qquad \text{Deviatoric back-stress} \\  \sigma_{y}, \sigma_{0} \qquad \text{Yield stress, initial} \\  \tau \qquad \text{Effective cohesive traction} \\  \tau_{\text{max}} \qquad \text{Tensile strength} \\  \tau_{\text{n}}, \tau_{\text{s}} \qquad \text{Normal and tangential cohesive traction} \\  \end{array}$		Damage					
$G_{\rm c}$ Critical energy release rate $G, G_{\rm c}, G_{\rm p}, G^{\rm max}, G^{\rm min}$ Energy release rate, elastic, plastic, maximum, minimum $K$ $K$ Stress intensity factor $K_{\rm c}$ Initial cohesive stiffness $I_{\rm p}$ Fracture process zone length $I_{\rm w}$ Weight function rate of decay $m, m_{\rm e}, m_{\rm p}$ Paris exponent, elastic, plastic $N$ Number of cycles $P, P_{\rm max}$ Applied load, maximum $Q_{\infty}$ Limit value for yield stress increase $R$ Radius $r_{\rm w}$ Weight function distance parameter $W$ Width $W$ Weighting value $S$ Deviatoric stress $S$ Deviatoric stress $S$ Deviatoric stress $S$ Mixed-mode strength ratio $S$ Non-linear kinematic hardening coefficient $S_{\rm t}, \delta_{\rm t}, \delta_{\rm m}$ Effective displacement jump, final failure, initiation, maximum $S_{\rm m}, S_{\rm s}$ Normal and tangential displacement jump $S_{\rm m}, S_{\rm s}$ Deviatoric back-stress $S_{\rm s}$ Deviatoric	$\boldsymbol{E}$	Young's modulus					
$G, G_c, G_p, G^{\max}, G^{\min}$ Energy release rate, elastic, plastic, maximum, minimum $K$ Stress intensity factor $K_c$ Initial cohesive stiffness $I_p$ Fracture process zone length $I_w$ Weight function rate of decay $m, m_c, m_p$ Paris exponent, elastic, plastic $N$ Number of cycles $P, P_{\max}$ Applied load, maximum $Q_{\infty}$ Limit value for yield stress increase $R$ Radius $r_w$ Weight function distance parameter $W$ Width $w$ Weighting value $s$ Deviatoric stress $\beta$ Mixed-mode strength ratio $\gamma$ Non-linear kinematic hardening coefficient $\delta, \delta_i, \delta_i, \delta_m$ Effective displacement jump, final failure, initiation, maximum $\delta_n, \delta_s$ Normal and tangential displacement jump $\epsilon^p$ Plastic strain $\epsilon^p$ Equivalent plastic strain $v$ Poisson ratio $\xi$ Deviatoric back-stress $\sigma_{\gamma}, \sigma_0$ Yield stress, initial $\tau$ Effective cohesive traction $\tau_{\max}$ Tensile strength $\tau_{\min}$ Normal and tangential cohesive traction	f	Von Mises yield criterion					
$K_c$ Stress intensity factor $K_c$ Initial cohesive stiffness $l_p$ Fracture process zone length $l_w$ Weight function rate of decay $m$ , $m_e$ , $m_p$ Paris exponent, elastic, plastic $N$ Number of cycles $P$ , $P_{max}$ Applied load, maximum $Q_{\infty}$ Limit value for yield stress increase $R$ Radius $r_w$ Weight function distance parameter $W$ Width $w$ Weighting value $s$ Deviatoric stress $\beta$ Mixed-mode strength ratio $\gamma$ Non-linear kinematic hardening coefficient $\delta$ , $\delta_f$ , $\delta_i$ , $\delta_m$ Effective displacement jump, final failure, initiation, maximum $\delta$ , $\delta_f$ , $\delta_i$ , $\delta_m$ Effective displacement jump, final failure, initiation, maximum $\delta$ , $\delta_f$ Normal and tangential displacement jump $e^p$ Plastic strain $\xi^p$ Equivalent plastic strain $\psi$ Poisson ratio $\xi$ Deviatoric back-stress $\sigma_y$ , $\sigma_0$ Yield stress, initial $\tau$ Effective cohesive traction	$G_{ m c}$	Critical energy release rate					
$K_c$ Initial cohesive stiffness $I_p$ Fracture process zone length $I_w$ Weight function rate of decay $m$ , $m_e$ , $m_p$ Paris exponent, elastic, plastic $N$ Number of cycles $P$ , $P_{\text{max}}$ Applied load, maximum $Q_{\infty}$ Limit value for yield stress increase $R$ Radius $r_w$ Weight function distance parameter $W$ Width $w$ Weighting value $s$ Deviatoric stress $\beta$ Mixed-mode strength ratio $\gamma$ Non-linear kinematic hardening coefficient $\delta$ , $\delta_t$ , $\delta_i$ , $\delta_m$ Effective displacement jump, final failure, initiation, maximum $\delta_n$ , $\delta_s$ Normal and tangential displacement jump $\epsilon^p$ Plastic strain $\epsilon^p$ Equivalent plastic strain $v$ Poisson ratio $\xi$ Deviatoric back-stress $\sigma_y$ , $\sigma_0$ Yield stress, initial $\tau$ Effective cohesive traction $\tau_{\text{max}}$ Tensile strength $\tau_n$ , $\tau_s$ Normal and tangential cohesive traction	$G, G_{\rm e}, G_{\rm p}, G^{\rm max}$	, $G^{\min}$ Energy release rate, elastic, plastic, maximum, minimum					
$\begin{array}{lll} I_{\rm p} & & & & & & \\ I_{\rm w} & & & & & & \\ Weight function rate of decay \\ m, m_{\rm e}, m_{\rm p} & & & & & \\ Number of cycles \\ P, P_{\rm max} & & & & \\ Applied load, maximum \\ Q_{\infty} & & & & \\ Limit value for yield stress increase \\ R & & & \\ Radius \\ r_{\rm w} & & & \\ Weight function distance parameter \\ W & & & \\ Width \\ w & & & \\ Weighting value \\ s & & & \\ Deviatoric stress \\ \beta & & \\ Mixed-mode strength ratio \\ \gamma & & \\ Non-linear kinematic hardening coefficient \\ \delta_{\gamma}, \delta_{\gamma}, \delta_{\gamma}, \delta_{m} & & \\ Effective displacement jump, final failure, initiation, maximum \\ \delta_{n}, \delta_{s} & & \\ Normal and tangential displacement jump \\ e^{\rho} & & \\ Plastic strain \\ \bar{\epsilon}^{\rho} & & \\ Equivalent plastic strain \\ v & & \\ Poisson ratio \\ \xi & & \\ Deviatoric back-stress \\ \sigma_{y}, \sigma_{0} & & \\ Yield stress, initial \\ \tau & & \\ Effective cohesive traction \\ \tau_{\rm max} & & \\ Tensile strength \\ \tau_{\rm n}, \tau_{\rm s} & & \\ Normal and tangential cohesive traction \\ \end{array}$	K	Stress intensity factor					
$l_{w}$ Weight function rate of decay $m$ , $m_{e}$ , $m_{p}$ Paris exponent, elastic, plastic $N$ Number of cycles $P$ , $P_{max}$ Applied load, maximum $Q_{\infty}$ Limit value for yield stress increase $R$ Radius $r_{w}$ Weight function distance parameter $W$ Width $w$ Weighting value $s$ Deviatoric stress $s$ Deviatoric stress $s$ Mixed-mode strength ratio $s$ Non-linear kinematic hardening coefficient $s$ , $s$ , $s$ , $s$ , $s$ , $s$ , Normal and tangential displacement jump $s$ , $s$ , $s$ , $s$ , Normal strength $s$ ,	$K_{\rm c}$	Initial cohesive stiffness					
$m, m_e, m_p$ Paris exponent, elastic, plastic $N$ Number of cycles $P, P_{\text{max}}$ Applied load, maximum $Q_{\infty}$ Limit value for yield stress increase $R$ Radius $r_{\text{w}}$ Weight function distance parameter $W$ Width $w$ Weighting value $s$ Deviatoric stress $\beta$ Mixed-mode strength ratio $\gamma$ Non-linear kinematic hardening coefficient $\delta, \delta_f, \delta_i, \delta_m$ Effective displacement jump, final failure, initiation, maximum $\delta_n, \delta_s$ Normal and tangential displacement jump $\epsilon^p$ Plastic strain $\epsilon^p$ Equivalent plastic strain $v$ Poisson ratio $\xi$ Deviatoric back-stress $\sigma_y, \sigma_0$ Yield stress, initial $\tau$ Effective cohesive traction $\tau_{\text{max}}$ Tensile strength $\tau_n, \tau_s$ Normal and tangential cohesive traction	$l_{ m p}$	Fracture process zone length					
$N$ Number of cycles $P$ , $P_{\text{max}}$ Applied load, maximum $Q_{\infty}$ Limit value for yield stress increase $R$ Radius $r_{\text{w}}$ Weight function distance parameter $W$ Width $w$ Weighting value $s$ Deviatoric stress $\beta$ Mixed-mode strength ratio $\gamma$ Non-linear kinematic hardening coefficient $\delta$ , $\delta_{\rm f}$ , $\delta_{\rm i}$ , $\delta_{\rm m}$ Effective displacement jump, final failure, initiation, maximum $\delta_{\rm n}$ , $\delta_{\rm s}$ Normal and tangential displacement jump $e^{\rm P}$ Plastic strain $e^{\rm P}$ Equivalent plastic strain $v$ Poisson ratio $\xi$ Deviatoric back-stress $\sigma_{\rm y}$ , $\sigma_{\rm 0}$ Yield stress, initial $\tau$ Effective cohesive traction $\tau_{\rm max}$ Tensile strength $\tau_{\rm n}$ , $\tau_{\rm s}$ Normal and tangential cohesive traction	$l_{ m w}$	Weight function rate of decay					
$P$ , $P_{\text{max}}$ Applied load, maximum $Q_{\infty}$ Limit value for yield stress increase $R$ Radius $r_{\text{w}}$ Weight function distance parameter $W$ Width $w$ Weighting value $\mathbf{s}$ Deviatoric stress $\beta$ Mixed-mode strength ratio $\gamma$ Non-linear kinematic hardening coefficient $\delta$ , $\delta_{\mathbf{f}}$ , $\delta_{\mathbf{i}}$ , $\delta_{\mathbf{m}}$ Effective displacement jump, final failure, initiation, maximum $\delta_{\mathbf{n}}$ , $\delta_{\mathbf{s}}$ Normal and tangential displacement jump $\epsilon^{\mathbf{p}}$ Plastic strain $\epsilon^{\mathbf{p}}$ Equivalent plastic strain $\mathbf{v}$ Poisson ratio $\xi$ Deviatoric back-stress $\sigma_{\mathbf{y}}$ , $\sigma_{0}$ Yield stress, initial $\tau$ Effective cohesive traction $\tau_{\text{max}}$ Tensile strength $\tau_{\mathbf{n}}$ , $\tau_{\mathbf{s}}$ Normal and tangential cohesive traction	$m, m_e, m_p$	Paris exponent, elastic, plastic					
$\begin{array}{lll} Q_{\infty} & \text{Limit value for yield stress increase} \\ R & \text{Radius} \\ r_{\text{w}} & \text{Weight function distance parameter} \\ W & \text{Width} \\ w & \text{Weighting value} \\ \mathbf{s} & \text{Deviatoric stress} \\ \beta & \text{Mixed-mode strength ratio} \\ \gamma & \text{Non-linear kinematic hardening coefficient} \\ \delta,  \delta_{\text{f}},  \delta_{\text{i}},  \delta_{\text{m}} & \text{Effective displacement jump, final failure, initiation, maximum} \\ \delta_{\text{n}},  \delta_{\text{s}} & \text{Normal and tangential displacement jump} \\ \epsilon^{\text{p}} & \text{Plastic strain} \\ \bar{\epsilon}^{\text{p}} & \text{Equivalent plastic strain} \\ v & \text{Poisson ratio} \\ \bar{\xi} & \text{Deviatoric back-stress} \\ \sigma_{\text{y}},  \sigma_{0} & \text{Yield stress, initial} \\ \bar{\tau} & \text{Effective cohesive traction} \\ \tau_{\text{max}} & \text{Tensile strength} \\ \tau_{\text{n}},  \tau_{\text{s}} & \text{Normal and tangential cohesive traction} \\ \end{array}$		·					
$R$ Radius $r_{\rm w}$ Weight function distance parameter $W$ Width $w$ Weighting value $s$ Deviatoric stress $\beta$ Mixed-mode strength ratio $\gamma$ Non-linear kinematic hardening coefficient $\delta$ , $\delta_{\rm f}$ , $\delta_{\rm i}$ , $\delta_{\rm m}$ Effective displacement jump, final failure, initiation, maximum $\delta_{\rm n}$ , $\delta_{\rm s}$ Normal and tangential displacement jump $\epsilon^{\rm p}$ Plastic strain $\epsilon^{\rm p}$ Equivalent plastic strain $v$ Poisson ratio $\xi$ Deviatoric back-stress $\sigma_{\rm y}$ , $\sigma_0$ Yield stress, initial $\tau$ Effective cohesive traction $\tau_{\rm max}$ Tensile strength $\tau_{\rm n}$ , $\tau_{\rm s}$ Normal and tangential cohesive traction	$P$ , $P_{\text{max}}$	Applied load, maximum					
$ \begin{array}{lll} r_{\rm w} & \mbox{Weight function distance parameter} \\ W & \mbox{Width} \\ w & \mbox{Weighting value} \\ {\bf s} & \mbox{Deviatoric stress} \\ \beta & \mbox{Mixed-mode strength ratio} \\ \gamma & \mbox{Non-linear kinematic hardening coefficient} \\ \delta,  \delta_{\rm f},  \delta_{\rm i},  \delta_{\rm m} & \mbox{Effective displacement jump, final failure, initiation, maximum} \\ \delta_{\rm n},  \delta_{\rm s} & \mbox{Normal and tangential displacement jump} \\ \epsilon^{\rm p} & \mbox{Plastic strain} \\ \epsilon^{\rm p} & \mbox{Equivalent plastic strain} \\ \nu & \mbox{Poisson ratio} \\ \xi & \mbox{Deviatoric back-stress} \\ \sigma_{\rm y},  \sigma_{\rm 0} & \mbox{Yield stress, initial} \\ \tau & \mbox{Effective cohesive traction} \\ \tau_{\rm max} & \mbox{Tensile strength} \\ \tau_{\rm n},  \tau_{\rm s} & \mbox{Normal and tangential cohesive traction} \\ \end{array}$	$Q_{\infty}$						
$\begin{array}{lll} W & \text{Width} \\ w & \text{Weighting value} \\ \mathbf{s} & \text{Deviatoric stress} \\ \beta & \text{Mixed-mode strength ratio} \\ \gamma & \text{Non-linear kinematic hardening coefficient} \\ \delta,  \delta_{\mathbf{f}},  \delta_{\mathbf{i}},  \delta_{\mathbf{m}} & \text{Effective displacement jump, final failure, initiation, maximum} \\ \delta_{\mathbf{n}},  \delta_{\mathbf{s}} & \text{Normal and tangential displacement jump} \\ \epsilon^{\mathbf{p}} & \text{Plastic strain} \\ \epsilon^{\mathbf{p}} & \text{Equivalent plastic strain} \\ v & \text{Poisson ratio} \\ \xi & \text{Deviatoric back-stress} \\ \sigma_{\mathbf{y}},  \sigma_{0} & \text{Yield stress, initial} \\ \tau & \text{Effective cohesive traction} \\ \tau_{\text{max}} & \text{Tensile strength} \\ \tau_{\mathbf{n}},  \tau_{\mathbf{s}} & \text{Normal and tangential cohesive traction} \\ \end{array}$	R	Radius					
$w$ Weighting value $s$ Deviatoric stress $\beta$ Mixed-mode strength ratio $\gamma$ Non-linear kinematic hardening coefficient $\delta$ , $\delta_f$ , $\delta_i$ , $\delta_m$ Effective displacement jump, final failure, initiation, maximum $\delta_n$ , $\delta_s$ Normal and tangential displacement jump $\epsilon^p$ Plastic strain $\bar{\epsilon}^p$ Equivalent plastic strain $\nu$ Poisson ratio $\xi$ Deviatoric back-stress $\sigma_y$ , $\sigma_0$ Yield stress, initial $\tau$ Effective cohesive traction $\tau_{\text{max}}$ Tensile strength $\tau_n$ , $\tau_s$ Normal and tangential cohesive traction	$r_{ m w}$						
sDeviatoric stress $\beta$ Mixed-mode strength ratio $\gamma$ Non-linear kinematic hardening coefficient $\delta$ , $\delta_f$ , $\delta_i$ , $\delta_m$ Effective displacement jump, final failure, initiation, maximum $\delta_n$ , $\delta_s$ Normal and tangential displacement jump $\epsilon^p$ Plastic strain $\bar{\epsilon}^p$ Equivalent plastic strain $\nu$ Poisson ratio $\xi$ Deviatoric back-stress $\sigma_y$ , $\sigma_0$ Yield stress, initial $\tau$ Effective cohesive traction $\tau_{\text{max}}$ Tensile strength $\tau_n$ , $\tau_s$ Normal and tangential cohesive traction	W	Width					
$\begin{array}{lll} \beta & \text{Mixed-mode strength ratio} \\ \gamma & \text{Non-linear kinematic hardening coefficient} \\ \delta,  \delta_{\rm f},  \delta_{\rm i},  \delta_{\rm m} & \text{Effective displacement jump, final failure, initiation, maximum} \\ \delta_{\rm n},  \delta_{\rm s} & \text{Normal and tangential displacement jump} \\ \epsilon^{\rm p} & \text{Plastic strain} \\ \bar{\epsilon}^{\rm p} & \text{Equivalent plastic strain} \\ v & \text{Poisson ratio} \\ \bar{\xi} & \text{Deviatoric back-stress} \\ \sigma_{\rm y},  \sigma_{\rm 0} & \text{Yield stress, initial} \\ \bar{\tau} & \text{Effective cohesive traction} \\ \bar{\tau}_{\rm max} & \text{Tensile strength} \\ \bar{\tau}_{\rm n},  \bar{\tau}_{\rm s} & \text{Normal and tangential cohesive traction} \end{array}$	w	Weighting value					
$\begin{array}{lll} \gamma & & \text{Non-linear kinematic hardening coefficient} \\ \delta,  \delta_{\rm f},  \delta_{\rm i},  \delta_{\rm m} & & \text{Effective displacement jump, final failure, initiation, maximum} \\ \delta_{\rm n},  \delta_{\rm s} & & \text{Normal and tangential displacement jump} \\ \epsilon^{\rm p} & & \text{Plastic strain} \\ \bar{\epsilon}^{\rm p} & & \text{Equivalent plastic strain} \\ \nu & & \text{Poisson ratio} \\ \bar{\xi} & & \text{Deviatoric back-stress} \\ \sigma_{\rm y},  \sigma_{\rm 0} & & \text{Yield stress, initial} \\ \bar{\tau} & & \text{Effective cohesive traction} \\ \bar{\tau}_{\rm max} & & \text{Tensile strength} \\ \bar{\tau}_{\rm n},  \bar{\tau}_{\rm s} & & \text{Normal and tangential cohesive traction} \\ \end{array}$	S						
$\delta,  \delta_{\rm f},  \delta_{\rm i},  \delta_{\rm m}$ Effective displacement jump, final failure, initiation, maximum $\delta_{\rm n},  \delta_{\rm s}$ Normal and tangential displacement jump $\epsilon^{\rm p}$ Plastic strain Equivalent plastic strain $\epsilon^{\rm p}$ Equivalent plastic strain $\epsilon^{\rm p}$ Deviatoric back-stress $\epsilon^{\rm p}$ Deviatoric back-stress $\epsilon^{\rm p}$ Yield stress, initial $\epsilon^{\rm p}$ Effective cohesive traction $\epsilon^{\rm p}$ Effective cohesive traction $\epsilon^{\rm p}$ Tensile strength $\epsilon^{\rm p}$ Normal and tangential cohesive traction	β						
$\delta_{\rm n},  \delta_{\rm s}$ Normal and tangential displacement jump $\epsilon^{\rm p}$ Plastic strain Equivalent plastic strain $\nu$ Poisson ratio $\xi$ Deviatoric back-stress $\sigma_{\rm y},  \sigma_{\rm 0}$ Yield stress, initial $\tau$ Effective cohesive traction $\tau_{\rm max}$ Tensile strength $\tau_{\rm n},  \tau_{\rm s}$ Normal and tangential cohesive traction	-						
$\epsilon^{\rm p}$ Plastic strain $\epsilon^{\rm p}$ Equivalent plastic strain $\nu$ Poisson ratio $\xi$ Deviatoric back-stress $\sigma_{\rm y}, \sigma_0$ Yield stress, initial $\tau$ Effective cohesive traction $\tau_{\rm max}$ Tensile strength $\tau_{\rm n}, \tau_{\rm s}$ Normal and tangential cohesive traction							
$ar{\epsilon}^{\mathrm{p}}$ Equivalent plastic strain $\nu$ Poisson ratio $\xi$ Deviatoric back-stress $\sigma_{\mathrm{y}}, \sigma_{0}$ Yield stress, initial $\tau$ Effective cohesive traction $\tau_{\mathrm{max}}$ Tensile strength $\tau_{\mathrm{n}}, \tau_{\mathrm{s}}$ Normal and tangential cohesive traction							
$ v$ Poisson ratio $ \xi$ Deviatoric back-stress $ \sigma_y, \sigma_0 $ Yield stress, initial $ \tau$ Effective cohesive traction $ \tau_{\text{max}} $ Tensile strength $ \tau_{\text{n}}, \tau_{\text{s}} $ Normal and tangential cohesive traction							
$\xi$ Deviatoric back-stress $\sigma_{y}, \sigma_{0}$ Yield stress, initial $\tau$ Effective cohesive traction $\tau_{\max}$ Tensile strength $\tau_{n}, \tau_{s}$ Normal and tangential cohesive traction	$ar{\epsilon}^{ ext{p}}$	·					
$\sigma_{\rm y},\sigma_0$ Yield stress, initial $ au$ Effective cohesive traction $ au_{\rm max}$ Tensile strength $ au_{\rm n}, au_{\rm s}$ Normal and tangential cohesive traction	ν						
$ au_{ m max}$ Effective cohesive traction $ au_{ m max}$ Tensile strength $ au_{ m n},  au_{ m s}$ Normal and tangential cohesive traction	ξ						
$ au_{ m max}$ Tensile strength $ au_{ m n},   au_{ m s}$ Normal and tangential cohesive traction	$\sigma_{\rm y}$ , $\sigma_0$	,					
$ au_{\rm n},  au_{\rm s}$ Normal and tangential cohesive traction	τ						
	$ au_{ ext{max}}$						
$\phi$ Location parameter	$\tau_{\rm n},~\tau_{\rm s}$						
	$\phi$	Location parameter					

or macroscopic crack tip. The energy release rate (ERR) is determined by means of the J-integral, which is linked to the Paris equation to compute the fatigue crack growth rate. The present study takes the cohesive XFEM formulation from [28] as a starting point and investigates its validity for capturing the physics of fatigue crack growth under various loading conditions. Specifically, this paper is focused on the determination and calibration of the cohesive zone parameters in combination with the Paris equation to predict fatigue crack growth, with special attention for out-of-phase loading and bi-axial loading in combination with overloading.

The paper starts with an overview of the numerical framework followed by a description of the behaviour of the bulk material and the cohesive zone. Subsequently, the crack tip propagation criteria are discussed. Next, the fracture parameters are determined, in which the tensile strength and a set of plastic Paris parameters require calibration. Finally, two numerical examples are presented to validate the model and to show the objectivity of the parameters. The numerical examples include out-of-phase biaxial loading and in-phase biaxial loading with a single overload.

#### 2. Numerical framework

A cracked medium with an elastic–plastic bulk material, as shown in Fig. 1, is examined. The crack propagates due to an applied cyclic loading. The non-linear fracture process zone ahead of the physical crack tip is captured by means of a cohesive zone, which is illustrated in Fig. 2. The numerical crack, i.e. the XFEM discontinuity, extends beyond the physical crack tip to include the cohesive zone. The tip of the discontinuity is referred to as the numerical crack tip. The cohesive tractions are large near the numerical crack tip and are zero at the physical crack tip.

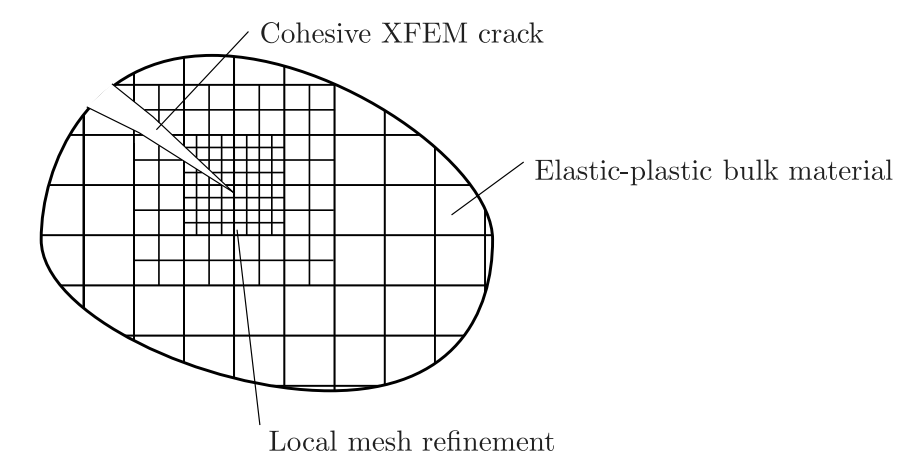


Fig. 1. Numerical framework.

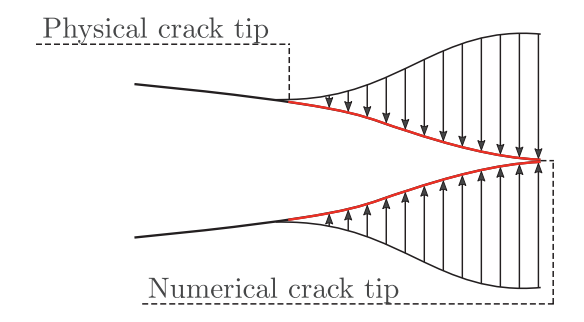


Fig. 2. Cohesive zone.

Fig. 1 also illustrates two characteristics of the numerical framework upon which the fatigue crack growth model is built. Both aspects follow from not knowing the crack path a priori. Firstly, there is the ability of XFEM for a discontinuity to be present along a non-predefined crack path running through the elements. Secondly, in order to correctly capture the crack tip behaviour, small elements are required in this region. However, when it is unknown where the crack will grow, small elements are required everywhere, which increases computation time significantly. This is addressed by making use of an adaptive meshing technique [29–31], which ensures the use of small elements only around the crack tip and larger elements elsewhere in order to improve computational efficiency.

## 3. Material behaviour

The bulk material and the cohesive zone both have their own set of constitutive relations. Consequently, the interaction between the bulk material and the cohesive zone dictates the crack growth behaviour. This section first describes the relations used for the bulk material, followed by those employed for the cohesive zone.

## 3.1. Bulk material

A bulk material having an elastic–plastic material response is considered. The elastic response is captured using Hooke's law which requires the Young's modulus E and the Poisson ratio v. The plastic response is modelled using both isotropic and kinematic hardening such that plastic flow under cyclic loading can be captured. The yield surface is described by means of the Von Mises criterion:

$$f = \sqrt{\frac{2}{3}(\mathbf{s} - \xi) : (\mathbf{s} - \xi)} - \sigma_{\mathbf{y}} \tag{1}$$

where s is the deviatoric stress and  $\xi$  the deviatoric back-stress. A non-linear isotropic hardening rule [32] is used to described the evolution of the yield stress  $\sigma_v$ :

$$\sigma_{y} = \sigma_{0} + Q_{\infty} \left( 1 - e^{-b\bar{\epsilon}^{p}} \right) \tag{2}$$

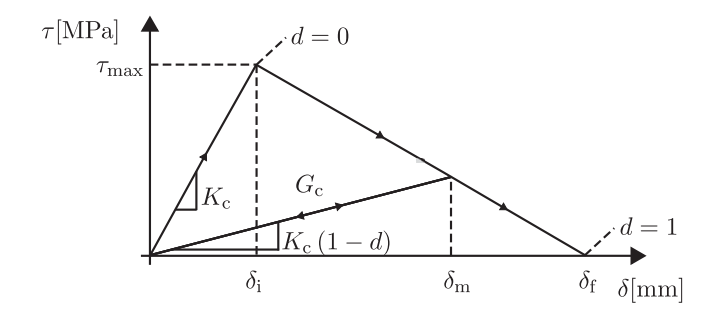


Fig. 3. Bilinear cohesive law.

where  $\sigma_0$  and  $Q_{\infty}$  are the initial yield stress and the limit value for the yield stress increase, respectively. The measure for the rate of change of the yield surface is indicated by b. The equivalent plastic strain increment  $\mathrm{d}\bar{e}^\mathrm{p}$  is a function of the plastic strain increment  $\mathrm{d}e^\mathrm{p}$ :

$$d\bar{\epsilon}^p = \sqrt{\frac{2}{3}} d\epsilon^p : d\epsilon^p$$
 (3)

The kinematic hardening rule is defined as [33]:

$$d\xi = \sum_{i=1}^{2} \left( \frac{2}{3} C_i d\epsilon^p - \gamma_i \xi_i d\bar{\epsilon}^p \right) \tag{4}$$

where  $\gamma_i$  is the non-linear kinematic hardening coefficient and  $C_i$  is the linear one.

#### 3.2. Cohesive zone model

In the cohesive zone model each integration point on the crack is assigned a static cohesive law from which the traction and the stiffness degradation through a damage parameter are computed. Fig. 3 shows the bilinear cohesive law that is used in this study.

A mixed-mode formulation is used in which the effective traction  $\tau$  is a function of the effective displacement jump  $\delta$ , which is defined as [34,35]:

$$\delta = \sqrt{\langle \delta_{\rm n} \rangle^2 + \beta^2 \delta_{\rm s}^2} \tag{5}$$

where  $\beta$  is equal to the ratio between the tensile and shear strength of the material. The normal and tangential displacement jumps are indicated by  $\delta_n$  and  $\delta_s$ , respectively.

The maximum effective traction stress  $\tau_{\text{max}}$  is equal to the material tensile strength and the critical ERR for mode I, indicated by  $G_{\text{c}}$ , is equal to the area under the curve of the cohesive law. The maximum effective displacement jump that has been reached by a material point on the crack is defined by  $\delta_{\text{m}}$ , which has a corresponding damage d that is given by:

$$d = \frac{\delta_{\rm f} \left( \delta_{\rm m} - \delta_{\rm i} \right)}{\delta_{\rm m} \left( \delta_{\rm f} - \delta_{\rm i} \right)} \quad \text{for } \delta_{\rm m} \ge \delta_{\rm i} \tag{6}$$

from which follows that an increase in  $\delta_{\rm m}$  results in an increase in d. Here,  $\delta_{\rm i}$  is the fracture initiation displacement jump and  $\delta_{\rm f}$  the final failure displacement jump, which are computed from the values of  $\tau_{\rm max}$ ,  $G_{\rm c}$  and the initial cohesive stiffness  $K_{\rm c}$ .

The damage starts to increase once the effective displacement jump exceeds  $\delta_i$  and reaches its maximum value of one for a displacement jump equal to  $\delta_f$ .  $K_c$  is multiplied with (1-d) to account for the accumulated damage. As a results, the effective traction–displacement relations are given by:

$$\tau = \begin{cases} K_{\rm c} \delta & \delta_{\rm m} < \delta_{\rm i} \\ K_{\rm c} (1 - d) \delta & \delta_{\rm m} \ge \delta_{\rm i} \\ 0 & \delta_{\rm m} \ge \delta_{\rm f} \end{cases}$$

$$(7)$$

The tractions in the normal direction  $\tau_n$  and sliding or tangential direction  $\tau_s$  are computed from the effective traction:

$$\tau_{n} = \begin{cases} \frac{\tau}{\delta_{m}} \delta_{n} & \delta_{n} \ge 0 \\ K_{c} \delta_{n} & \delta_{n} < 0 \end{cases}$$
(8)

$$\tau_{\rm s} = \beta^2 \frac{\tau}{\delta} \delta_{\rm s} \tag{9}$$

The initial cohesive stiffness is used to calculate the normal traction in the case of a negative displacement jump, irrespective of the value of accumulated damage. Contact between the two crack faces is ensured by means of a large initial stiffness which ensures that

any negative normal displacement jumps remain small. Consequently,  $K_c$  should be sufficiently large such that the global response is not influenced by its exact value.

Extraction of the ERR is done by computing the J-integral around the interface elements by integrating the traction–separation relation along the fracture process zone following Bak et al. [36]:

$$G = -\int_0^{l_p} \tau \frac{\partial \delta}{\partial \phi} d\phi \tag{10}$$

where  $I_p$  is the total length of the cohesive zone and  $\phi$  the variable that runs from 0 at the physical crack tip to  $I_p$  at the numerical crack tip. For a fully developed cohesive zone, as obtained during quasi-static crack growth, this G is equal to  $G_c$ . However, for fatigue crack growth G is generally lower than  $G_c$ .

#### 3.3. Fatigue crack relation

The crack growth rate is computed by means of the Paris equation [37]:

$$\frac{\mathrm{d}a}{\mathrm{d}N} = c \left(\Delta K\right)^m \tag{11}$$

where N is the number of cycles, a is the crack length and  $\Delta K$  is the Stress Intensity Factor (SIF) range. The Paris constant and exponent are indicated by c and m.

The cohesive zone gives the ERR for a given state of the model. For elastic materials the SIF can simply be converted to the ERR by means of the following equation:

$$K = \sqrt{EG} \tag{12}$$

which is only valid for the state of plane stress, although a comparable relation exists for plane strain as well.

The effective displacement jump defined in Eq. (5) is used to capture the effect of different mode-mixities on *G*. Consequently, the mode I Paris parameters are used to determine the fatigue crack growth rate for mixed-mode loading as well. Potentially, the model can be expanded to include roughness induced crack closure by adjusting the cohesive zone behaviour. Plugging Eq. (12) into Eq. (11) gives the Paris relation as a function of the ERR:

$$\frac{\mathrm{d}a}{\mathrm{d}N} = c_{\mathrm{e}} \left( \sqrt{EG_{\mathrm{e}}^{\mathrm{max}}} - \sqrt{EG_{\mathrm{e}}^{\mathrm{min}}} \right)^{m_{\mathrm{e}}} \tag{13}$$

where the subscript  ${\bf e}$  has been added to the Paris parameters and the ERR  ${\bf G}$  to indicate that it concerns an elastic bulk material.

Note that Eq. (12) does not result in a real SIF in the case of an elastic-plastic material. Nonetheless, the SIF computed from the ERR for the fracture process zone inside the elastic-plastic bulk material could still potentially be used as a measure for the magnitude of the crack driving force. Therefore, for an elastic-plastic bulk material, Eq. (13) is written as:

$$\frac{\mathrm{d}a}{\mathrm{d}N} = c_{\mathrm{p}} \left( \sqrt{EG_{\mathrm{p}}^{\mathrm{max}}} - \sqrt{EG_{\mathrm{p}}^{\mathrm{min}}} \right)^{m_{\mathrm{p}}} \tag{14}$$

where the parameters  $c_{\rm p}$  and  $m_{\rm p}$  require calibration. The subscript p is added to indicate that it holds for an elastic–plastic bulk material. Unlike the  $c_{\rm e}$  and  $m_{\rm e}$  from Eq. (13),  $c_{\rm p}$  and  $m_{\rm p}$  cannot be directly identified from experiments as there is no method to measure  $G_{\rm p}$  from experimental observations. It should be mentioned that the common approach where K is related to the force through linear elastic fracture mechanics (LEFM) relations is not without problems either as LEFM theory fails to capture measured stress ratio effects, let alone crack retardation through overloading. In contrast, the  $G_{\rm p}$  from Eq. (14) is a quantity that accounts for the shielding effect of the plastic zone.

#### 4. Crack tip propagation

Fig. 4 illustrates a cohesive crack in a finite element mesh in which the locations of the numerical and physical crack tip, as well as the cohesive integration points and the regular integration points for several elements are indicated. The arc length of the fracture process zone, indicated with the solid line, is equal to  $l_p$ . Complete separation of the crack faces, i.e. damage equal to one, is indicated by the thick dashed line. The magnitude of  $l_p$  is determined based on the position of the physical and the numerical crack tip, which both have their own criterion of propagation. The length of the fracture process zone changes as the crack propagates due to the changing stress field around the crack tip. It is noted that both crack tips are only allowed to grow from element boundary to element boundary.

The numerical crack tip propagates through one element when the maximum principal stress  $\sigma_I$  in any integration point located in a small region around the numerical crack tip exceeds the failure stress. The failure stress is equal to  $\tau_{max}$  in Fig. 3 and acts as a numerical quantity rather than the value extracted from a 1D tensile test. The small region is taken to have a radius of three times the element size and is indicated in Fig. 4 with the circle around the numerical crack tip. The crack growth direction is computed using the maximum principal stress criterion [38], using a non-local approach [39]. The non-local stress is computed by weighing the state of stress of each integration point located in the neighbourhood of the numerical crack tip with the following equation:

$$w = \frac{l_{\rm w}}{(2\pi)^{3/2} l_{\rm w}^3} \exp\left(-\frac{r_{\rm w}^2}{2l_{\rm w}^2}\right) \tag{15}$$

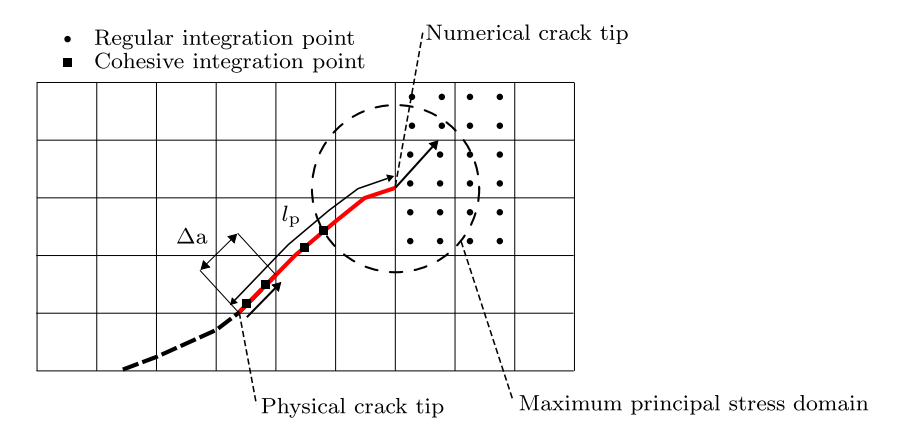


Fig. 4. A crack (dashed line) with fracture process zone (solid line) in an extended finite element model framework. Note that this figure is only an illustration. Cohesive integration points are present along the whole crack and regular integration throughout the whole domain.

Table 1 Elastic paris parameters [3].	
$c_{ m e}$	$m_{\mathrm{e}}$
6.78e-8	3.32

Here,  $r_{\rm w}$  and  $l_{\rm w}$  are the distance from the numerical crack tip to the considered integration point and the rate of decay of the weight function, respectively. The arrow from the numerical crack tip in Fig. 4 indicates a possible propagation direction.

To obtain fatigue crack growth at  $G < G_c$ , the physical crack tip is forced forward by a crack length increment  $\Delta a$  by setting the damage value of the process zone element that is next to the current physical crack tip equal to one [40,41]. The physical crack tip is following the path defined by the numerical discontinuity, as indicated by the arrow from the physical crack tip also shown in Fig. 4. The propagation process of the physical crack tip is performed after each simulated loading cycle. At the post-processing stage, the actual amount of fatigue cycles  $\Delta N$  that each simulated loading cycle represents is calculated by means of Eq. (14) for an elastic–plastic or Eq. (13) for an elastic material, which requires  $\Delta a$ ,  $G^{\max}$  and  $G^{\min}$  to be known. The crack growth length  $\Delta a$  is equal to the distance the physical crack tip needs to be shifted forward to reach the next element edge, and  $G^{\max}$  and  $G^{\min}$  are known because the ERR is evaluated at each time step during the simulated cycle and thus the effective stress intensity range is known as well. By computing the ERR at every time step, it is not necessary to inform the part of the code where the ERR is computed about when boundary conditions are at a maximum or minimum, or even to assume that  $G^{\max}$  is synchronized with maximum boundary conditions which would for instance not be the case in the presence of viscoelasticity.

A flow diagram of the whole crack propagation process is given in Fig. 5. Initially the physical crack tip and the numerical crack tip coincide, which means that the simulation starts with a sharp notch without cohesive zone. The numerical produce starts with setting the applied loading or loadstep, after which a finite element calculation is performed to compute the displacements, strains and stresses. First, it is monitored if numerical crack tip propagation should be performed. If this is not the case, it will be checked if the current loadstep is the final step of a fatigue load cycle. If this criterion is not met, the ERR is computed and a new load step is introduced. If one of the two criteria is met, either numerical crack tip or physical crack tip propagation is performed, followed by a mesh adaptivity process. More details on the mesh refinement can be found in [28]. The displacements, strains and stresses are then calculated for the same loadstep for this new configuration. Note that it is only possible to meet the cycle end criterion only once for a specific loadstep. Furthermore, a 3D implementation for the current crack growth algorithm is possible following Moes et al. [42,43].

## 5. Model calibration

Model calibration is performed on the fatigue crack growth experiments reported by Zhao et al. [3] for a 7075-T6 aluminium alloy. The tests were executed on the compact tension specimen given in Fig. 6 with a width W of 50.8 mm and a thickness of 4.76 mm. The crack has an initial length a of 12.8 mm. The applied cyclic load has a load ratio of 0.1 and a maximum applied load  $P_{\rm max}$  of 3 kN. The problem is considered to be in a state of plane stress. The elastic Paris parameters resulting from these tests are given in Table 1. Note that these elastic Paris parameters are computed on the assumption that linear elastic fracture mechanics can be used.

The presented numerical model includes plasticity parameters and cohesive law parameters. The plasticity parameters are obtained from Naderi et al. [44] and are given in Table 2. The cohesive law parameters, which should be calibrated, include the cohesive stiffness  $K_c$ , the critical ERR  $G_c$  and the tensile strength  $\tau_{\text{max}}$ . Baseline values of the cohesive zone parameters are given in Table 2 as well, where the parameter  $\beta$  as well as  $G_c$  follow from [45]. These baseline values are used in the numerical simulations presented in this paper except when mentioned otherwise. Furthermore, the plastic Paris parameters require calibration as well. The calibration of the cohesive law parameters  $K_c$ ,  $G_c$  and  $\tau_{\text{max}}$ , and the Paris parameters  $m_p$  and  $c_p$  will be discussed next.

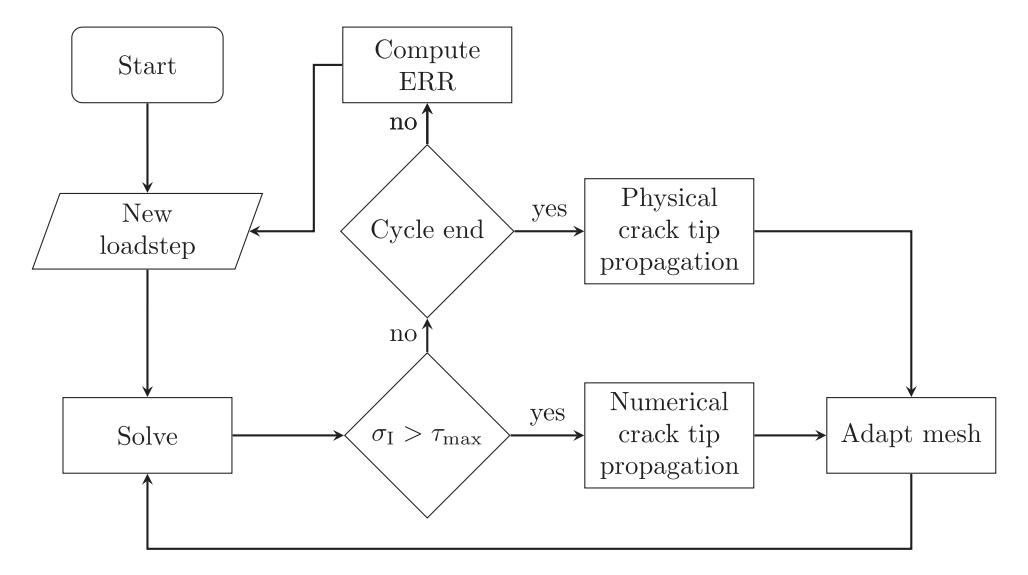


Fig. 5. Flow diagram of the fatigue crack propagation model.

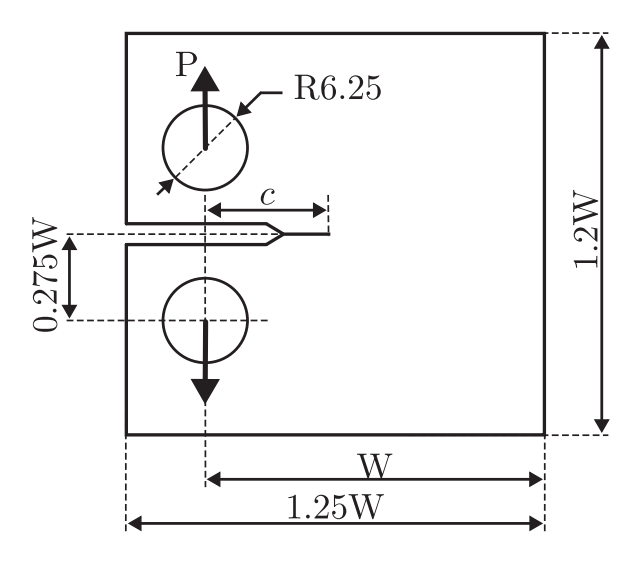


Fig. 6. Compact tension specimen.

## 5.1. Cohesive stiffness

The value of  $K_c$ , if chosen sufficiently stiff, should not influence the global response. In order to prove this, a simulation under constant amplitude fatigue loading on the CTS, as defined above, has been performed for varying values of cohesive stiffness. In Fig. 7a the computed ERR is plotted as a function of the crack length, which shows that the effect of the cohesive stiffness on the results is negligible for all values larger or equal to  $10^8 \, \text{N/mm}^3$ . However, it should be mentioned that choosing a too large value could result in non-convergence of the solution.

#### 5.2. Critical energy release rate

The value of  $G_c$  can be determined experimentally. However, its value depends on the material grain direction as well as the amount of plasticity around the crack tip during the test, resulting in different sources giving different values [45–47]. In the present framework where plasticity is separately represented,  $G_c$  should not include energy dissipation in the plastic region around the fracture process zone. The value of this parameter is mainly important to determine when fatigue crack growth turns into crack growth under monotonic loading. As shown in Fig. 7b, a change in  $G_c$  results in a minimal change in  $G_c$  Furthermore, because the Paris parameters and  $G_c$  still need to be calibrated after choosing the values for  $G_c$ , it is safe to assume that the exact value of  $G_c$  does not influence the fatigue behaviour. As mentioned before, the  $G_c$  used in this study is taken from [45].

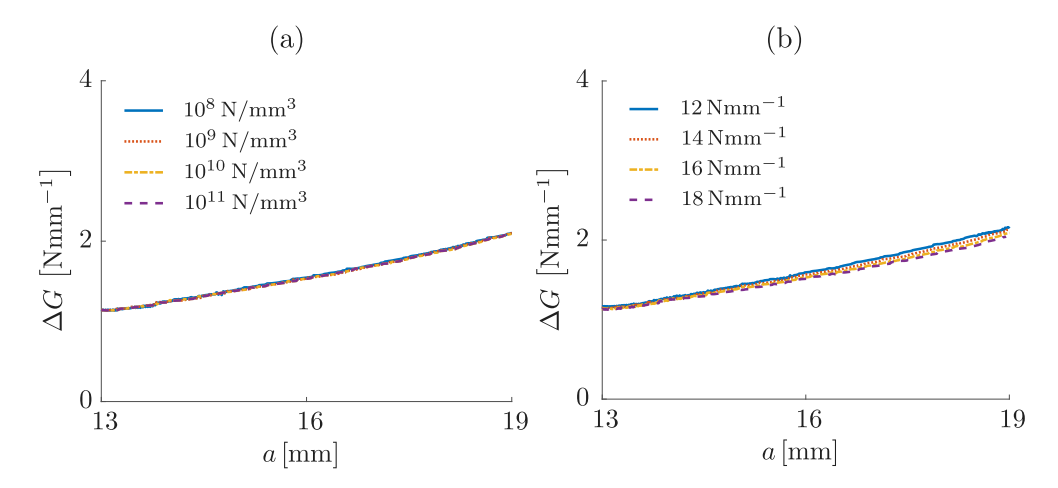


Fig. 7. ERR range for different values of (a)  $K_c$  and (b)  $G_c$ .

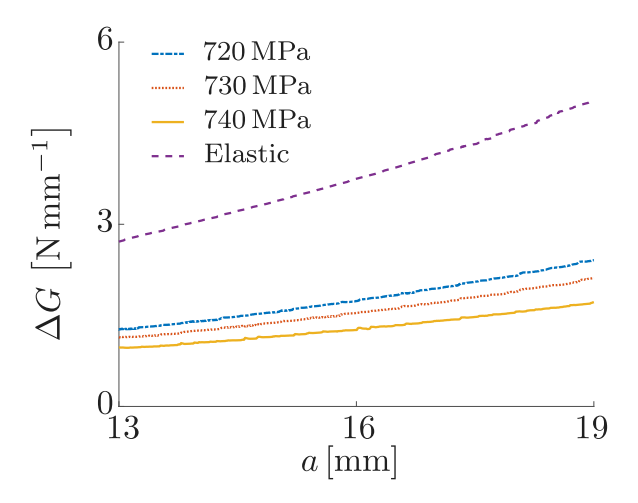


Fig. 8. ERR range as function of  $\tau_{max}$ .

## 5.3. Tensile strength and Paris parameters

For fatigue crack growth simulations three parameters remain that require calibration, namely the Paris constant and exponent, and  $\tau_{\rm max}$ . However, these parameters are not independent of each other. This is illustrated in Fig. 8, which shows the influence of  $\tau_{\rm max}$  on the ERR range. A higher  $\tau_{\rm max}$  allows for larger strains and therefore a larger plastic zone, which reduces the ERR. Note that  $\tau_{\rm max}$  acts as a calibration parameter and its value does not necessarily have a physical meaning. For reference, the curve for an elastic bulk material is added as well, which can be obtained by an empirical relation [48] or numerically, independent of  $\tau_{\rm max}$ . In the case with elastic bulk material, a value for  $\tau_{\rm max}$  of 1200 MPa has been used, although in absence of plasticity results are insensitive to the strength as long as it results in a cohesive zone that is sufficiently small compared to specimen dimensions and yet spans several finite elements

For each value of  $\tau_{max}$ , the Paris parameters can be calibrated to a Paris curve, see Eq. (13), with the elastic Paris parameters given in Table 1 as input by means of a least square minimization. It should be emphasized that each value of  $\tau_{max}$  has its own tuned set of Paris parameters, which all give the same crack growth rate in the case of constant amplitude loading.

The model parameters cannot be uniquely identified with data from a constant amplitude test. At this point it is still unknown which set of  $\tau_{max}$  and Paris parameters should be selected. This selection follows from simulating an overload case, where the data is again taken from an experiment done by Zhao et al. [3]. In this experiment, an overload of 6 kN, which is twice the maximum load in the constant amplitude part, was applied at a crack length of 14.96 mm. Note with respect to the simulation scheme shown in Fig. 5, this overload is a single cycle, and thus no physical crack propagation is done immediately after the overload. First, a constant amplitude load cycle is run before physical crack propagation is performed again.

For every combination of  $\tau_{max}$  and corresponding Paris parameters, a different amount of crack retardation is obtained when the overload case is simulated. The set that is able to quantitatively capture the experimentally observed retardation effect is selected.

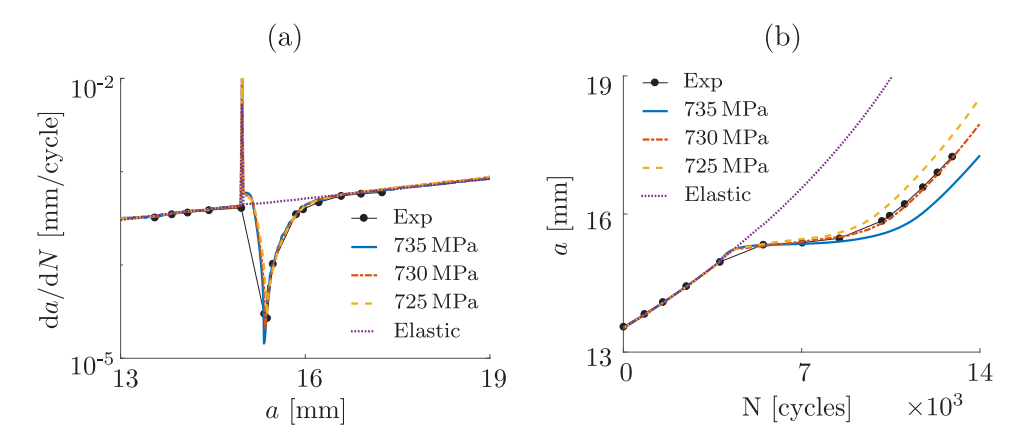


Fig. 9. (a) Crack growth rate and (b) number of fatigue cycles for different tensile strength compared against a mode I fatigue overload experiment (Exp) [3].

Table 2 Model parameters.									
E	ν	$\sigma_0$	$Q_{\infty}$	b	$C_1$	$C_2$	$\gamma_1$	$\gamma_2$	
70.94 GPa	0.33	420 MPa	140 MPa	40	175 GPa	9 GPa	3500	180	

Fig. 9 shows crack growth results from simulations where the overload experiment is modelled using different values of  $\tau_{max}$  and their respective Paris parameters, as well as using an elastic bulk material as a reference. It can be seen that all parameter sets give a good match with the experiment for the constant amplitude part, while only the parameter set with  $\tau_{max}$  equal to 730 MPa agrees with the experimental retardation behaviour. A higher value for  $\tau_{max}$  results in too much retardation and a lower value in too little. The elastic material results only in a peak in crack growth rate at the moment the overload is applied, but afterwards no effect is observed, as was expected. In Fig. 9a it can also be observed that the retardation is preceded by a short period of crack acceleration right after the application of the overload. The resolution of experimental measurements is not sufficient to determine whether this effect was also present in the test. However, depending on the material and loading conditions, crack growth acceleration after an overload is not uncommon [49]. Finally, note that the optimal combination of  $\tau_{max}$  and Paris parameters depends on the chosen plasticity parameters, of which different values can be found in literature [44,50,51]. Also, the numerical fracture process zone length for the specified calibration case is found to be in the order of 0.1 mm.

$ au_{ ext{max}}$	β	$G_{\rm c}$	$K_{\rm c}$	$c_{ m p}$	$m_{\mathrm{p}}$
730 MPa	1.73	$14.5  \mathrm{N}  \mathrm{mm}^{-1}$	$10^8  \text{N/mm}^3$	$2.32\times10^{-7}$	3.29

#### 6. Validation

Fatigue simulations for biaxial fatigue loading are performed and the results are compared against experimental data from literature [5,52] to investigate whether the calibrated model is valid for more complex load scenarios as well. The tests were performed on the same material as the tests used for the calibration of the model in the previous section. All validation tests consider the notched cruciform specimen given in Fig. 10, which has a rounded square section around the centre which has a smaller thickness t compared to the rest of the specimen. Biaxial cyclic loading is applied where the load cycles in the two directions are either in-phase or out-of-phase with a predefined phase shift. In the case of out-of-phase loading, the vertical load is lagging behind the horizontal one. The numerical analyses are performed using the model parameters from Table 2 as calibrated in Section 5. Furthermore, the same analyses are also executed for an elastic bulk material in order to investigate the influence of plasticity. After that, a bi-axial overload example is simulated and compared against experimental observations. For all these analyses a state of plane stress is assumed.

#### 6.1. Constant amplitude loading

The experimental data for the constant amplitude biaxial fatigue loading examples are taken from literature [5,52]. Three different types of loading are considered, namely, in-phase loading (IP),  $45^{\circ}$  out-of-phase loading (OP45) and  $90^{\circ}$  out-of-phase loading (OP90). The loading ratio is equal to 0.1 and the maximum applied load in both directions is equal to  $15 \, \text{kN}$ .

The experimental data consist out of two or three different runs of the same experiment with considerable scatter between the different runs as shown in Fig. 11a. This scatter can be substantially reduced when starting to count the fatigue cycles from a slightly larger crack length as shown in Fig. 11b, demonstrating a certain initiation life, which could be caused by variation in the notch geometry between different specimens. Therefore, the crack growth results are shown from a crack length of 2 mm to ensure that the numerical model is compared to the experiments for the fatigue crack propagation stage and excluding the fatigue initiation stage.

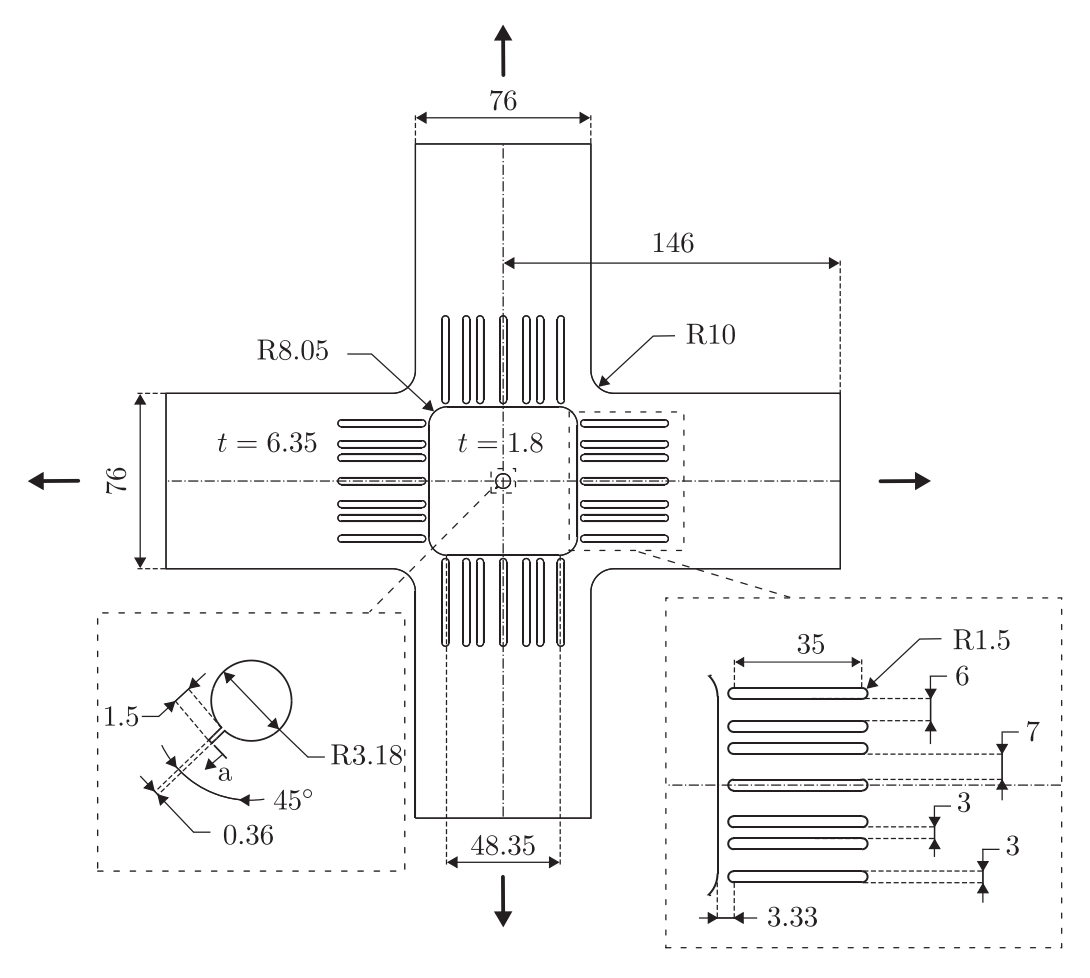


Fig. 10. Geometry of cruciform specimen (Dimensions are in millimetres).

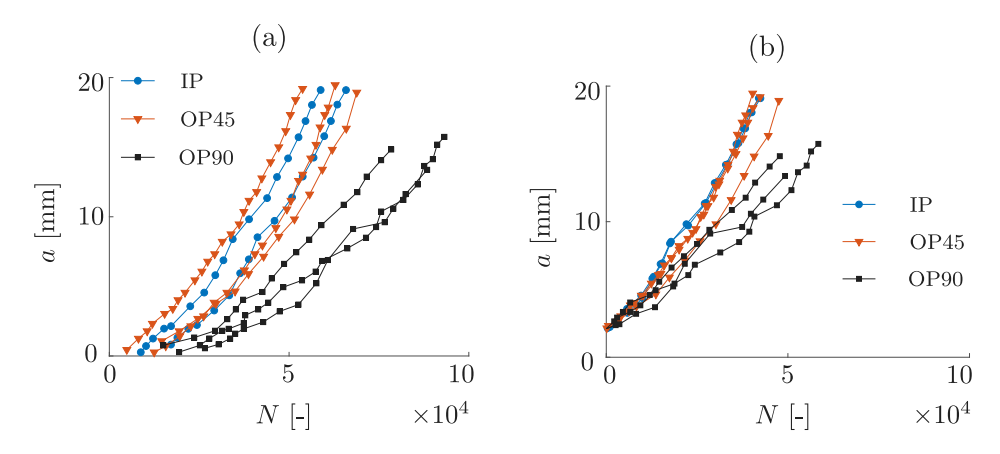


Fig. 11. Experimental crack growth data [5,52] (a) without adjustment and (b) taking 2 mm as a starting point for the fatigue cycle count.

## 6.1.1. Elastic-plastic bulk material

The comparison of the crack path between the numerical model (Num), employing an elastic–plastic bulk material, and the experimental data (Exp) is shown in Fig. 12a. Only one crack path per loading condition is given in the articles containing the experimental data. The crack path for IP and OP90 show reasonable agreement. It is surprising that experimentally the crack path for OP45 does not lie between the crack paths for OP90 and IP. The simulations do not reproduce this.

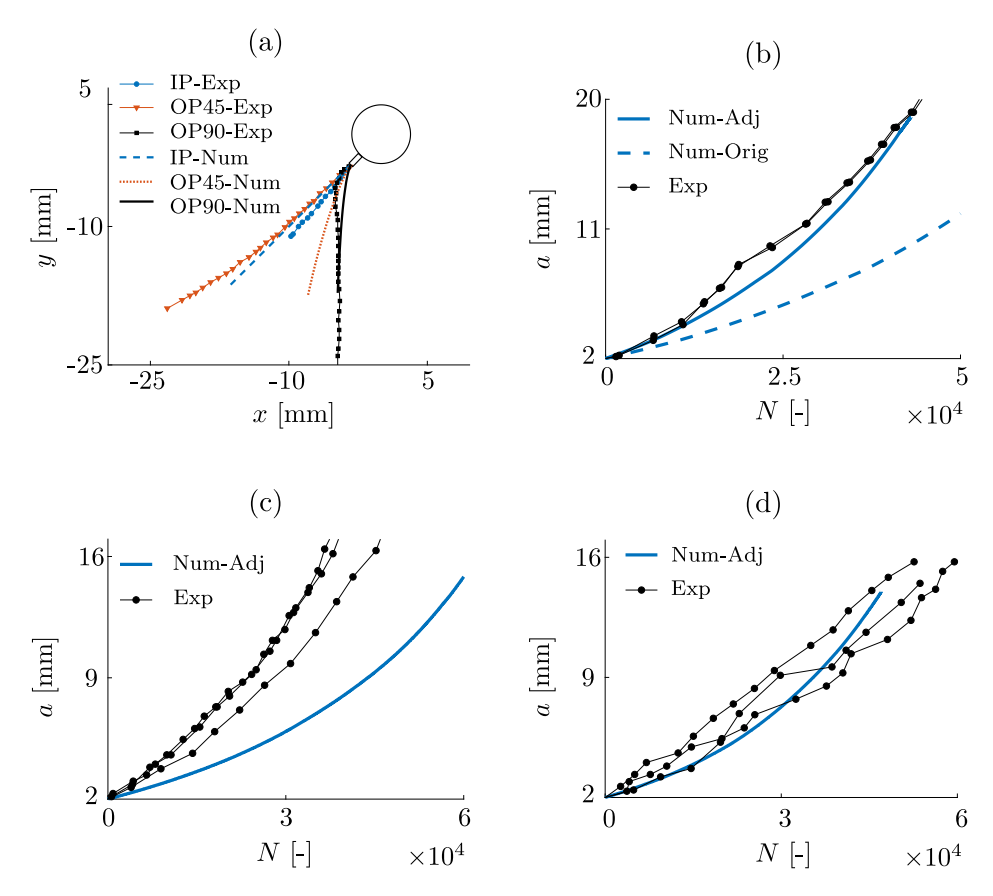


Fig. 12. (a) The crack paths and the amount of fatigue cycles for (b) IP,(c) OP45 and (d) OP90 according to the numerical model (Num), using an elastic-plastic bulk material, and experiment (Exp).

Next, Fig. 12b shows the comparison of crack growth as a function of number of load cycles. Here, two lines are included from the numerical model. The dashed line is the result of using the original (orig) plastic Paris parameters previously calibrated on the CTS. It can be seen that the number of cycles required to reach a specific crack length is significantly over-predicted with these parameters. This could possibly be attributed to a difference in batch material or a difference in production process between the two specimens.

Here, increasing the Paris constant by 55% for the cruciform specimen to  $c_{\rm p}=3.6\times 10^{-7}$  leads to a good agreement for IP loading between the numerical model and the experiment. The newly calibrated Paris constant is used in the following simulations of different cases with the same geometry: OP45, OP90 and IP overload. Using this adjusted (adj) Paris constant for in-phase loading results in the solid line in Fig. 12b, which now shows there is good agreement. Note that re-calibration of the Paris parameters does not affect the crack path in the simulations, because the Paris equation is only used in post-processing to compute the number of cycles required per crack increment.

There is a relatively poor agreement between numerical model and experiment for OP45 as shown in Fig. 12c, which could be expected with the already observed mismatch in crack path. On the other hand, Fig. 12d shows a good agreement with the experiment for OP90.

## 6.1.2. Elastic bulk material

The same comparison of the numerical model with experiment has been performed considering an elastic bulk material. Here, the Paris parameters from Table 1 are used. The comparison in crack path is given in Fig. 13a. Again, IP and OP90 match relatively well with the experiments while OP45 does not.

Also for the elastic bulk material, using parameters calibrated on the compact tension specimen does not result in a good match in crack growth as function of number of cycles, which is shown by the dashed line in Fig. 13b. Again, in order for the in-phase loading case to agree with the experiment the Paris constant is increased. For the elastic bulk material the Paris constant is increased by 31% to  $c_{\rm e}=8.88\times10^{-8}$ . The solid line in Fig. 13b shows the cycles versus crack length for the adjusted Paris constant, which now follows the experiment.

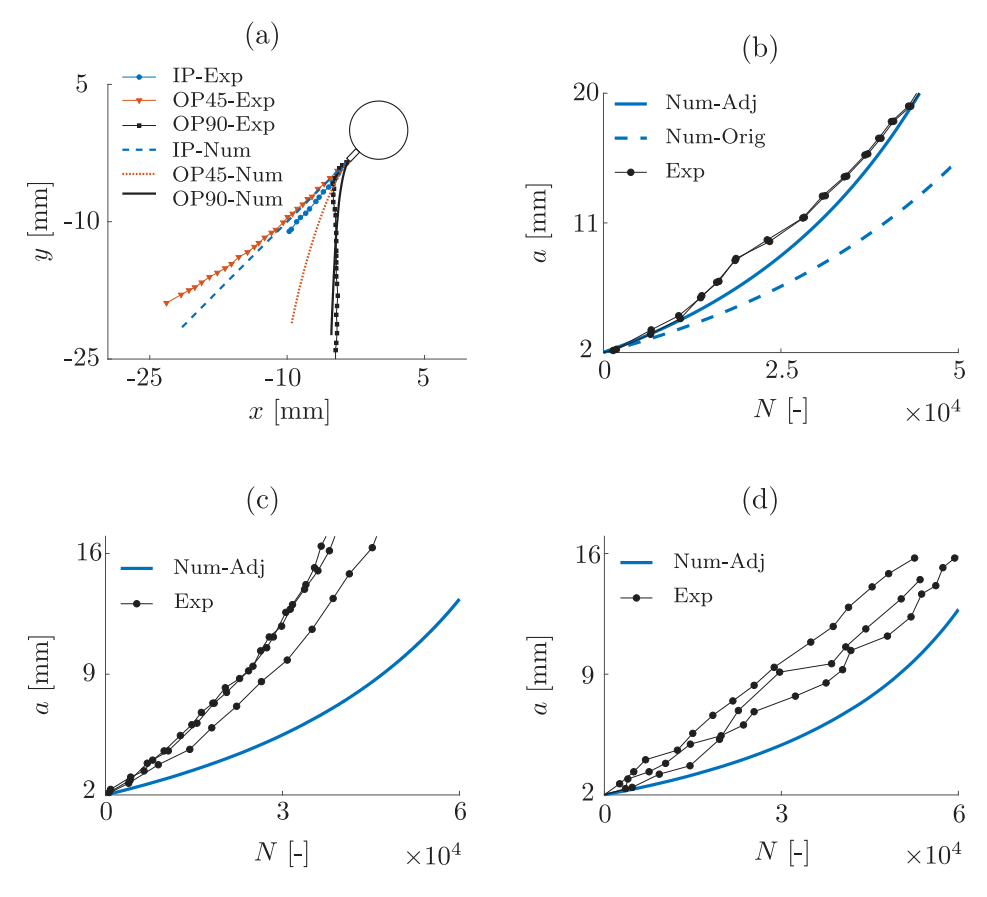


Fig. 13. (a) The crack paths and the amount of fatigue cycles for (b) IP,(c) OP45 and (d) OP90 according to the numerical model (Num), using an elastic bulk material, and experiment (Exp).

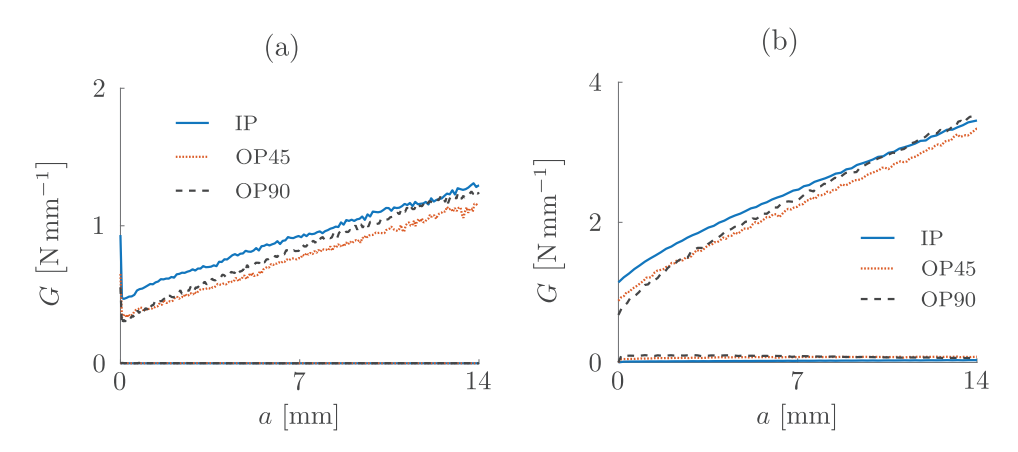


Fig. 14. The minimum and maximum ERR versus crack length for (a) the elastic-plastic and (b) the elastic bulk material.

The solid lines Figs. 13c and 13d show the crack growth behaviour using the adjusted Paris constant for OP45 and OP90, respectively. Interestingly, neither is in agreement with the experiment, while for the elastic–plastic bulk material OP90 did agree with the experiment. This indicates the need to include elastic–plastic material behaviour when considering out-of-phase loading.

Fig. 14 shows the maximum and minimum ERR for the elastic–plastic and the elastic bulk material. It can be seen that the  $G^{min}$  for the elastic–plastic bulk material is zero for all crack lengths due to plasticity induced crack closure. This is not the case for the elastic material, which could potentially explain why using an elastic bulk material in the numerical analyses cannot capture the correct crack growth rate for OP90.

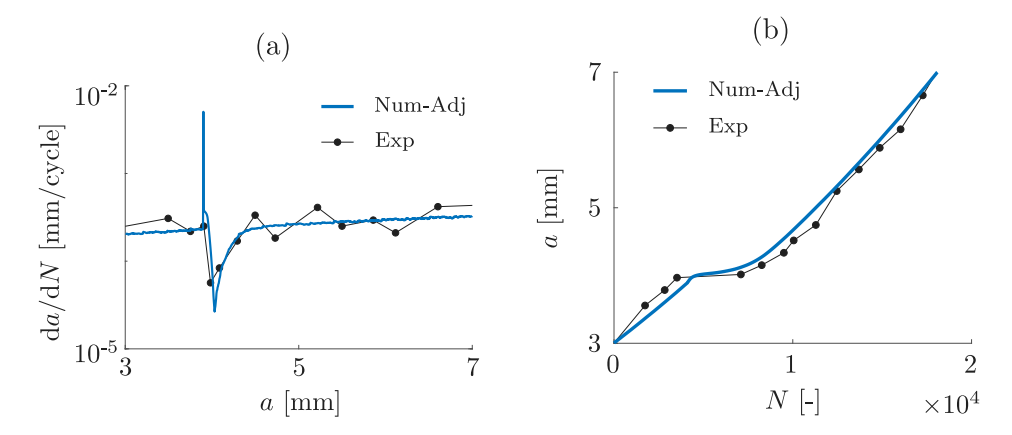


Fig. 15. (a) The crack growth rate and (b) the amount of fatigue cycles according to the numerical model (Num), using an elastic-plastic bulk material and the adjusted Paris constant, and experiment.

## 6.2. Biaxial loading with a single overload

The experimental data for the bi-axial overloading example is taken from the same work by Datta et al. [52] from which also one of the constant amplitude in-phase loading experimental curves discussed before originated. Therefore, the adjusted Paris constant should also be valid for the overload case. The loading ratio is equal to 0.1 and the maximum applied load is equal to 15 kN, which is the same as in the constant amplitude case. The overload is introduced at a crack length of 3.9 mm and has an amplitude of 1.75 times the maximum applied load.

The comparison between experiment and the numerical model is given in Fig. 15. It can be seen that both the crack growth rate and the amount of cycles show good agreement. It is emphasized that accurately capturing the constant amplitude part as well as the retardation did not require recalibration of the strength parameter as determined for the thicker compact tension specimen.

#### 7. Conclusions

This study discussed in detail the calibration and validation of a cohesive XFEM model for fatigue crack growth simulations in ductile materials based on the authors' earlier work [28]. It is shown that the cohesive stiffness does not influence the energy release rate for a given crack length. Furthermore, the fatigue behaviour is independent of the critical energy release rate. Contrary to most other cohesive zone models described in literature, this study provides a consistent procedure to calibrate all parameters involved. In total three parameters required calibration: the Paris constant, the Paris exponent and the tensile strength. Increasing the tensile strength results in a lower energy release rate for a given crack length. For every value of the tensile strength, the plastic Paris parameters can be calibrated to a constant amplitude cyclic loading test. After that, the correct set of tensile strength and Paris parameters is chosen such that it can correctly capture crack retardation in an overload experiment.

The calibrated parameters are subsequently used for in-phase and out-of-phase bi-axial loading problems on a cruciform specimen made of a ductile material, from which the experimental data originate from a different source in literature. In terms of crack path, in which the Paris parameters do not play a role, there was a good agreement with experiment for in-phase loading and 90° out-of-phase loading. However, the numerical model showed a deviation from the crack path in the experiment for 45° out-of-phase loading. Recalibrating the Paris constant, such that the numerical model agreed with the experiment for in-phase biaxial loading, resulted in a good agreement for 90° out-of-phase biaxial loading and biaxial loading with a single overload for experiments on the same geometry. It was not necessary to calibrate the strength parameter to accurately reproduce the retardation observed in the experiment.

The importance of including plasticity for fatigue crack growth was illustrated with numerical results obtained with the same cohesive zone model but then embedded in a linear elastic bulk material. With the elastic bulk material, no crack retardation after overloading is obtained. Moreover, parameters resulting in a good agreement with the experiment for in-phase biaxial loading do not result in a good agreement in out-of-phase biaxial loading or overloading. It is concluded that including elastic-plastic material behaviour is essential when numerically investigating fatigue crack growth under load conditions that deviate from most simple constant amplitude mode I cases.

## Declaration of competing interest

The authors declare that they have no known competing financial interests or personal relationships that could have appeared to influence the work reported in this paper.

#### Acknowledgements

This research is part of the EUROS program, which is supported by NWO domain Applied and Engineering Sciences and partly funded by the Dutch Ministry of Economic Affairs.

#### References

- [1] Elber W. Fatigue crack closure under cyclic tension. Eng Fract Mech 1970;2(1):37-45.
- [2] Elber W. The significance of fatigue crack closure. In: Damage Tolerance in Aircraft Structures. ASTM International; 1971.
- [3] Zhao T, Zhang J, Jiang Y. A study of fatigue crack growth of 7075-T651 aluminum alloy. Int J Fatigue 2008;30(7):1169-80.
- [4] Oian J, Fatemi A. Mixed mode fatigue crack growth: A literature survey. Eng Fract Mech 1996;55(6):969-90.
- [5] Neerukatti RK, Datta S, Chattopadhyay A, Iyyer N, Phan N. Fatigue crack propagation under in-phase and out-of-phase biaxial loading. Fatigue Fract Eng Mater Struct 2017:41:387–99.
- [6] Yang B, Mall S, Ravi-Chandar K. A cohesive zone model for fatigue crack growth in quasibrittle materials. Int J Solids Struct 2001;38(22):3927-44.
- [7] Nguyen O, Repetto EA, Ortiz M, Radovitzky RA. A cohesive model of fatigue crack growth. Int J Fract 2001;110(4):351-69.
- [8] Roe KL, Siegmund T. An irreversible cohesive zone model for interface fatigue crack growth simulation. Eng Fract Mech 2003;70(2):209-32.
- [9] Ural A, Krishnan VR, Papoulia KD. A cohesive zone model for fatigue crack growth allowing for crack retardation. Int J Solids Struct 2009;46(11):2453-62.
- [10] Jiang H, Gao X, Srivatsan TS. Predicting the influence of overload and loading mode on fatigue crack growth: A numerical approach using irreversible cohesive elements. Finite Elem Anal Des 2009;45(10):675–85.
- [11] Silitonga S, Maljaars J, Soetens F, Snijder HH. Numerical simulation of fatigue crack growth rate and crack retardation due to an overload using a cohesive zone model. In: 11th International Fatigue Congress. Advanced Materials Research, vol. 891, Trans Tech Publications; 2014, p. 777–83.
- [12] Belytschko T, Black T. Elastic crack growth in finite elements with minimal remeshing. Internat J Numer Methods Engrg 1999;45(5):601-20.
- [13] Moës N, Dolbow J, Belytschko T. A finite element method for crack growth without remeshing. Internat J Numer Methods Engrg 1999;46(1):131-50.
- [14] Singh IV, Mishra BK, Bhattacharya S, Patil RU. The numerical simulation of fatigue crack growth using extended finite element method. Int J Fatigue 2012;36(1):109-19.
- [15] Pathak H, Singh A, Singh IV. Fatigue crack growth simulations of 3-D problems using XFEM. Int J Mech Sci 2013;76:112-31.
- [16] Kumar M, Ahmad S, Singh IV, Rao AV, Kumar J, Kumar V. Experimental and numerical studies to estimate fatigue crack growth behavior of Ni-based super alloy. Theor Appl Fract Mech 2018;96:604–16.
- [17] Kumar M, Singh IV, Mishra BK. Fatigue crack growth simulations of plastically graded materials using XFEM and J-integral decomposition approach. Eng Fract Mech 2019;216:106470.
- [18] Plank R, Kuhn G. Fatigue crack propagation under non-proportional mixed mode loading. Eng Fract Mech 1999;62(2):203-29.
- [19] Lee EU, Taylor RE. Fatigue behavior of aluminum alloys under biaxial loading. Eng Fract Mech 2011;78:1555-64.
- [20] Mall S, Perel VY. Crack growth behavior under biaxial fatigue with phase difference. Int J Fatigue 2015;74:166-72.
- [21] Infante-García D, Qian G, Miguélez H, Giner E. Analysis of the effect of out-of-phase biaxial fatigue loads on crack paths in cruciform specimens using XFEM. Int J Fatigue 2019;123:87–95.
- [22] Voormeeren LO, van der Meer FP, Maljaars J, Sluys LJ. A new method for fatigue life prediction based on the thick level set approach. Eng Fract Mech 2017;182:449–66.
- [23] Hansbo A, Hansbo P. An unfitted finite element method, based on nitsche's method, for elliptic interface problems. Comput Methods Appl Mech Engrg 2002;191:5537–52.
- [24] Hansbo A, Hansbo P. A finite element method for the simulation of strong and weak discontinuities in solid mechanics. Comput Methods Appl Mech Engrg 2004;193:3523–40.
- [25] Mergheim J, Kuhl E, Steinmann P. A finite element method for the computational modelling of cohesive cracks. Internat J Numer Methods Engrg 2005;63(2):276–89.
- [26] Song JH, Areias PMA, Belytschko T. A method for dynamic crack and shear band propagation with phantom nodes. Internat J Numer Methods Engrg 2006;67(6):868-93.
- [27] van der Meer FP, Sluys LJ. A phantom node formulation with mixed mode cohesive law for splitting in laminates. Int J Fract 2009;158(2):107-24.
- [28] Dekker R, van der Meer FP, Maljaars J, Sluys LJ. A cohesive XFEM model for simulating fatigue crack growth under mixed-mode loading and overloading. Internat J Numer Methods Engrg 2019;118(10):561–77.
- [29] Palle N, Dantzig JA. An adaptive mesh refinement scheme for solidification problems. Metall Mater Trans A 1996;27(3):707-17.
- [30] Greaves DM, Borthwick AGL. Hierarchical tree-based finite element mesh generation. Internat J Numer Methods Engrg 1999;45(4):447-71.
- [31] Tabarraei A, Sukumar N. Adaptive computations on conforming quadtree meshes. Finite Elem Anal Des 2005;41(7):686–702, The Sixteenth Annual Robert J. Melosh Competition.
- [32] Chaboche JL. Constitutive equations for cyclic plasticity and cyclic viscoplasticity. Int J Plast 1989;5(3):247–302.
- [33] Chaboche JL. On some modifications of kinematic hardening to improve the description of ratchetting effects. Int J Plast 1991;7(7):661-78.
- [34] Meschke G, Dumstorff P. Energy-based modeling of cohesive and cohesionless cracks via X-FEM. Comput Methods Appl Mech Engrg 2007;196:2338-57.
- [35] Ruiz G, Pandolfi A, Ortiz M. Three-dimensional cohesive modeling of dynamic mixed-mode fracture. Internat J Numer Methods Engrg 2001;52:97–120.
- [36] Bak BLV, Turon A, Lindgaard E, Lund E. A simulation method for high-cycle fatigue-driven delamination using a cohesive zone model. Internat J Numer Methods Engrg 2015;106(3):163–91.
- [37] Paris P, Erdogan F. A critical analysis of crack propagation laws. J. Basic Eng. 1963;85(4):528-33.
- [38] Erdogan F, Sih GC. On the crack extension in plates under plane loading and transverse shear. J Basic Eng 1963;85(4):519–27.
- [39] Wells GN, Sluys LJ. A new method for modelling cohesive cracks using finite elements. Internat J Numer Methods Engrg 2001;50(12):2667-82.
- [40] Harper PW, Hallett SR. A fatigue degradation law for cohesive interface elements development and application to composite materials. Int J Fatigue 2010;32(11):1774–87.
- [41] Iarve EV, Hoos K, Braginsky M, Zhou E, Mollenhauer DH. Progressive failure simulation in laminated composites under fatigue loading by using discrete damage modeling. J Compos Mater 2017;51(15):2143–61.
- [42] Moës N, Belytschko T. Extended finite element method for cohesive crack growth. Eng Fract Mech 2002;69(7):813-33.
- [43] Gravouil A, Moës N, Belytschko T. Non-planar 3D crack growth by the extended finite element and level sets part II: Level set update. Internat J Numer Methods Engrg 2002;53(11):2569–86.
- [44] Naderi M, Hoseini SH, Khonsari MM. Probabilistic simulation of fatigue damage and life scatter of metallic components. Int J Plast 2013;43:101-15.
- [45] Davis JR, editor. Metals handbook. ASM International; 1998.
- [46] Zinkham RE. Anisotropy and thickness effects in fracture of 7075-T6 and -T651 aluminum alloy. Eng Fract Mech 1968;1(2):275-6.
- [47] DuQuesnay DL, Underhill PR, Britt HJ. Fatigue crack growth from corrosion damage in 7075-T6511 aluminium alloy under aircraft loading. Int J Fatigue 2003:25:371-7.

- [48] Anderson TL. Fracture mechanics: Fundamentals and applications. Taylor and Francis; 2005.
- [49] Sadananda K, Vasudevan AK, Holtz RL, Lee EU. Analysis of overload effects and related phenomena. Int J Fatigue 1999;21:S233 S246.
- [50] Agius D, Wallbrink C, Hu W, Kajtaz M, Wang CH, Kourousis KI. On the utilisation of nonlinear plasticity models in military aircraft fatigue estimation: A preliminary comparison. Aerosp Sci Technol 2017;71:25–9.
- [51] Agius D, Kajtaz M, Kourousis KI, Wallbrink C, Wang CH, Hu W, Silva J. Sensitivity and optimisation of the chaboche plasticity model parameters in strain-life fatigue predictions. Mater Des 2017;118:107–21.
- [52] Datta S, Chattopadhyay A, Iyyer N, Phan N. Fatigue crack propagation under biaxial fatigue loading with single overloads. Int J Fatigue 2018;109:103–13.